

Pile-up Reduction, Bayesian Decomposition and Applications of Silicon Drift Detectors at LCLS

G. Blaj*, *Member, IEEE*, C. J. Kenney, *Member, IEEE*, A. Dragone, G. Carini, *Member, IEEE*, S. Herrmann, P. Hart, A. Tomada, *Member, IEEE*, J. Koglin, G. Haller, *Member, IEEE*, S. Boutet, M. Messerschmidt, G. Williams, M. Chollet, G. Dakovski, S. Nelson, J. Pines, S. Song, J. Thayer

Abstract—Silicon drift detectors (SDDs) revolutionized spectroscopy in fields as diverse as geology and dentistry. For a subset of experiments at ultra-fast, x-ray free-electron lasers (FELs), SDDs can make substantial contributions. Often the unknown spectrum is interesting, carrying science data, or the background measurement is useful to identify unexpected signals. Many measurements involve only several discrete photon energies known a priori, allowing single event, Bayesian decomposition of pile-up and spectroscopic photon counting. We designed a pulse function (a combination of gradual step and exponential decay function) and demonstrated that for individual pulses the signal amplitude, peaking time, and pulse amplitude are interrelated and at short peaking times the pulse amplitude is not an optimal estimator for signal amplitude; instead, the signal amplitude and peaking time are obtained for each pulse by fitting, thus removing the need for pulse shaping. Avoiding pulse shaping reduced peaking times to tens of nanoseconds, resulting in reduced pulse pile-up and allowing decomposition of remaining pulse pile-up at photon separation times down to 100 ns while yielding time-of-arrival information with precision of 10 nanoseconds. At pulsed sources or high photon rates, photon pile-up still occurs. We showed that the area of one photon peaks is not suitable for estimating high photon rates while pile-up spectrum fitting is relatively simple and preferable to pile-up spectrum deconvolution. We developed a photon pile-up model for constant intensity sources, extended it to variable intensity sources (typical for FELs) and used it to fit a complex pile-up spectrum, demonstrating its accuracy. Based on the pile-up model, we developed a Bayesian pile-up decomposition method that allows decomposing pile-up of single events with up to 6 photons from 6 monochromatic lines with 99% accuracy. The usefulness of SDDs will continue into the x-ray FEL era of science. Their successors, the ePixS hybrid pixel detectors, already offer hundreds of pixels, each with similar performance to an SDD, in a compact, robust and affordable package.

Index Terms—Silicon drift detectors, free-electron lasers, pulse pile-up, photon pile-up, Bayesian decomposition, x-ray spectroscopy, photon counting

I. INTRODUCTION

Silicon drift detectors (SDDs) [1] are a well-established technology that has revolutionized spectroscopy in fields as

diverse as geology and dentistry. At a first glance it would seem that detectors with such a slow response would not be suitable for the new ultra-fast x-ray free-electron lasers (FEL) coming online [2]. However, FELs require a range of detectors with different requirements to cover the applications space [3], [4], [5]. For a subset of experiments at FELs, SDDs can make substantial contributions [6], [7].

Many measurements involve only several distinct photon energies known a priori, significantly simplifying photon pile-up analysis. Often the unknown spectrum is interesting, carrying science data, or the background measurement is useful to identify unexpected signals.

We investigate the performance of silicon drift detectors at x-ray FELs. In particular we study the ability to decompose the pile-up spectrum that results from various combinations of a few wavelengths and the possibility of separately recording photons that are absorbed at different radii (thus having varying drift times).

The typical approach to pulse processing in detection with a wide range of detectors (scintillation, gas, high purity germanium, SDD, transition edge) is to preamplify the detector signal, perform pulse shaping, and collect histograms of the resulting pulse peak heights [8].

When individual waveforms are (partially) overlapping, pulse pile-up occurs, modifying pulse height and resulting in spectrum distortion [9]. This can be classified in two broad classes: (1) long term, “tail” pile-up, resulting in resolution degradation (further called “pulse pile-up”); and (2) coincidences (overlapping in the peaking part), resulting mainly in sum distortion, further called “photon pile-up”.

Both pile-up mechanisms occur with increasing probability for larger pulse shaping and decay times. Short peaking times result in a noise increase (e.g., for SDDs, increasing hyperbolically with decreasing peaking times [10]).

To mitigate this problem, often pulse processors have a slow channel for energy resolution and a fast channel for time resolution and pile-up rejection [11]. Signals arriving within short time intervals will not be separated by the pile-up rejection and result in photon pile-up. Considerable effort has been invested on mathematical descriptions of spectrum distortion in the presence of pile-up and pile-up rejection (e.g., [9], [12]) and spectrum correction (e.g., [13], [14]).

As an alternative to pulse shaping of scintillator signals, [15] predicted dispensing with analog processing and using fast ADC conversion followed by software waveform fitting. By eliminating pulse shaping, the peaking time can be much

Manuscript received January 26, 2017; revised June 3, 2017. SLAC-PUB-16991.

G. Blaj, C. J. Kenney, A. Dragone, G. Carini, S. Herrmann, P. Hart, A. Tomada, J. Koglin, G. Haller, S. Boutet, M. Messerschmidt, G. Williams, M. Chollet, G. Dakovski, S. Nelson, J. Pines, S. Song, and J. Thayer are with SLAC National Accelerator Laboratory, Menlo Park, CA 94025, U.S.A.

A. Tomada is currently with the SRI International, Menlo Park, CA 94025, U.S.A., M. Messerschmidt is currently with the European XFEL, 22869 Schenefeld, Germany and G. Williams is currently with Brookhaven National Laboratory, Upton, NY 11973, U.S.A.

* Corresponding author: blaj@slac.stanford.edu.

shorter, significantly reducing pile-up. In current commercial pulse processors this partially came to fruition: while peak shaping is still being used, it is typically performed with digital filters in the frequency domain [16], reducing costs while taking advantage of current field-programmable gate arrays (FPGAs).

However, computing power, memory, storage and data transfer rates continue to improve, making it likely that pulse processing will continue to transition towards full software processing (taking advantage of increasing computation resources and fulfilling the promise of largely avoiding pulse pile-up). An added advantage is providing timestamps for individual photons which allows measuring coincidence in multiple detectors [15], or position information with pulsed sources, while enabling high rates of detection. Some photon pile-up will still occur (photons arriving at very short time intervals, or at pulsed sources).

For SDDs, different drift times result in different amounts of diffusion, and consequently, different peaking times. In the absence of peak shaping, these differences in peaking times are significant. We show that the signal, peak height and shaping times are interrelated; variation in peaking times of individual pulses must be taken into account in a function fit for optimal energy resolution in the absence of peak shaping.

As a consequence of the Poissonian counting statistic, the one photon peak area is a non-injective, nonlinear, peak-shaped function of the corresponding photon rate. For low rates, the peak area can be used to approximate the photon rate directly. At higher photon rates, the dependency becomes nonlinear, and beyond a certain point (rate $\lambda = 1$ photon/event) decreases. Measuring higher photon rates accurately benefit from using the pile-up peaks instead of deconvolving them.

We present here an accurate model for photon pile-up of discrete spectra with increasing complexity, from monochromatic through bicolor to general and use it for fitting a discrete spectrum, effectively deconvolving it. We further expand the model to include variable intensity sources with a gamma distribution, typical for, e.g., FEL sources.

Other approaches to single event Bayesian decomposition of photon pile-up use complex iterative Markov chain Monte Carlo [17] or χ^2 fitting [18]. Both are optimized for x-ray astronomy, expecting limited pile-up, complex spectra, and iteratively analyzing each event, updating the spectrum, and repeating until convergence. They are highly complex and relatively slow.

Using the photon pile-up model we developed a Bayesian pile-up decomposition method which yields the individual photon energies for each photon pile-up event and evaluate its accuracy to 99% for a spectrum with photon pile-up of up to 6 photons from 6 monochromatic lines.

II. METHODS

A. Experimental Set-up

The experiments were performed at the Linac Coherent Light Source (LCLS) at SLAC National Accelerator Laboratory. Two LCLS instruments were used, X-ray Pump-Probe (XPP) [19] and Coherent X-ray Imaging (CXI) [20]. Fig. 1

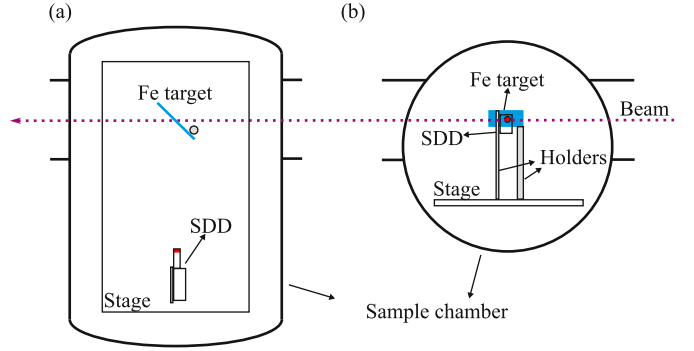


Fig. 1. Schematic diagram of the sample chamber at the Coherent X-ray Imaging instrument at LCLS: (a) top view: the direct beam passes through an Fe target and exits the chamber; fluorescence and scattered photons are collected at a right angle onto the silicon drift detector (SDD); the entire setup is enclosed in the vacuum chamber; (b) side view, showing the Fe target and SDD at beam height.

shows a schematic diagram of the CXI experimental chamber, with a Fe target and an SDD detector.

We projected FEL beam pulses of ≈ 9 keV photons on an Fe target (at FELs, the photon energy and beam intensity are somewhat variable from pulse to pulse), resulting in a detected signal composed of scattered 9 keV radiation together with Fe fluorescence (Fe $K\alpha$ at 6.40 keV and Fe $K\beta$ at 7.06 keV).

We used a standard Amptek XR-100SDD detector with a resolution of 125 eV full width at half maximum (FWHM) at 5.9 keV, an active area of 25 mm² and thickness of 500 μ m. In front of the SDD we mounted a collimator with two cylindrical apertures (0.5 mm diameter), placed over the SDD such that one aperture was aligned with the center of the SDD and the other was at a 2.5 mm radius towards the periphery of the SDD. We will subsequently refer them as the “central” and “peripheral” apertures.

Using collimators to convert standard SDDs to position sensitive detectors comes at the cost of reduced fill factor in our experiment, with each aperture passing about 0.8 % of the detector area. However, a large number of photons was present and the reduced fill factor was not an issue.

B. Waveform Acquisition and Processing

The SDD current was amplified and high-pass filtered with an Amptek PX5 Digital Pulse Processor [10] and its analog differentiator output was routed to the AUX1 analog port. The analog signal waveforms were then acquired by an Acquiris high-speed digitizer, with 8192 samples at 100 MHz for each FEL pulse and triggered pulse by pulse by the low jitter LCLS trigger signal. We will use the term “events” to refer to individual acquisitions from single FEL pulses. Each event resulted in one single waveform. We acquired 354 304 events and corresponding waveforms at 120 events per second.

The AUX1 analog signal of PX5 does not provide the analog prefilter output signal directly. Instead, it is digitized by the ADC at 80 MHz and subsequently synthesized by the DAC at 10 MHz [21]. This is clearly visible in the raw data, shown with small blue dots in Fig. 2; each DAC change results in a transient signal with an exponential decay from the current

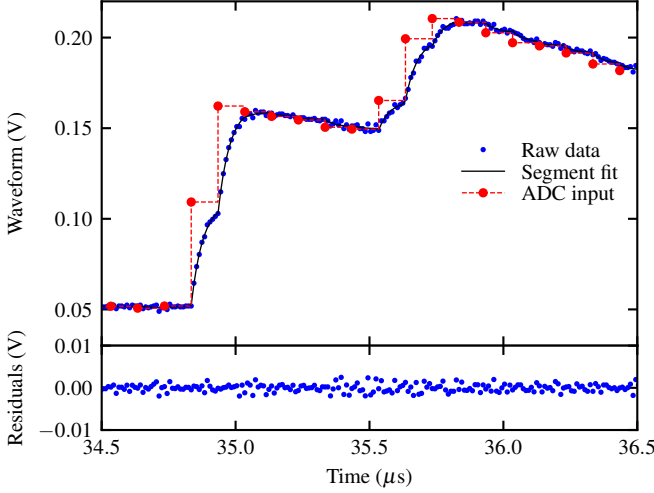


Fig. 2. Blue dots indicate a typical raw waveform of the Amptek PX5 analog prefilter, acquired at 100 MHz; the Amptek PX5 DAC only updates at 10 MHz, resulting in a series of 10 sample segments, each with an exponential decay towards its DAC target value; the black lines indicate the least squares fit for each segment, and the dashed red line with large red dots indicate the reconstruction of the DAC output, representing the analog prefilter output of the Amptek PX5; arrival times of $\approx 35 \mu\text{s}$ are calculated from arrival time $t_0 = 0$ of the FEL trigger signal.

output towards the target output. The time constant of the DAC exponential low pass filter is $\tau = 43.5 \text{ ns}$ in our setup.

To recover the initial signal from the transient exponential decay segments, we fitted each 100 ns (10 samples) segment of raw data between 2 DAC updates with an exponential decay:

$$y_{\text{raw}} = y_{\text{ADC}} + A e^{-\frac{t-t_0}{\tau}} \quad (1)$$

where t_0 is the time offset of the first sample in the current segment, y_{ADC} the new target output. The PX5 DAC and Acquisiris were not synchronized and their time offset changed in each waveform. However, the offset can be recovered from the data by using t_0 as a global waveform fitting parameter and minimizing χ^2 .

The resulting fit is indicated with a black line for one waveform in Fig. 2. The dashed red line and large red dots indicate the reconstructed time and amplitude of the DAC output, correcting for the system low pass filtering. Correcting distortions introduced by the ADC, DAC and exponential low pass filtering results in significantly improved results.

Arrival times are calculated from time $t = 0$ corresponding to the arrival of the trigger signal that precedes each FEL pulse, with $t \approx 35 \mu\text{s}$ determined by the experimental layout and cable lengths.

C. Pulse Function

The pulse height analysis can be optimally performed in the frequency domain [16]. Here we chose to perform the analysis in the time domain, allowing accurate reconstruction of timing, clipping and pile-up of pulses.

An individual pulse has a shape characterized by a relatively rapid increase near the arrival time t_0 and a relatively slow

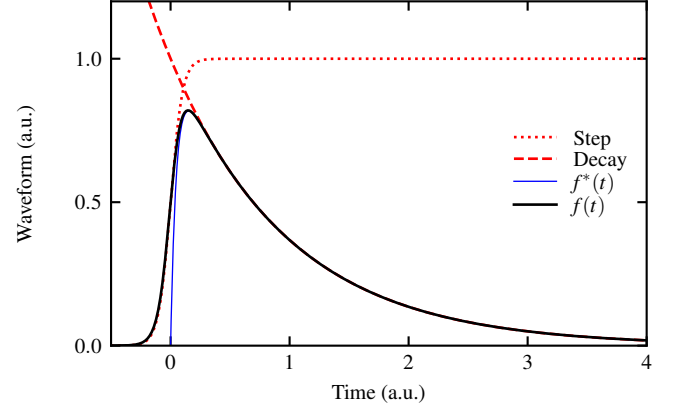


Fig. 3. Example of pulse function $f(x)$ (solid black line, Eq. 3) obtained by multiplying a gradual step function (dotted red line, Eq. 1) with an exponential decay (dashed red line, Eq. 8). For reference, a commonly used function with exponential peaking $f^*(t)$ is shown with a thin blue line.

exponential decay towards zero afterwards. An often used pulse function is:

$$f^*(t) = A \left(1 - e^{-\frac{t-t_0}{\tau_p}} \right) e^{-\frac{t-t_0}{\tau_d}} \quad (2)$$

which assumes that the peaking occurs as an exponential decay towards 1 with peaking time τ_p (first factor in Eq. 2) multiplied by an exponential decay with decay time τ_d (second factor in Eq. 2). The typical pulse function $f^*(t)$ is illustrated in Fig. 3 by the thin blue line.

After high-pass filtering in the analog prefilter, and in the absence of peak shaping, peaking is fast, with a slower onset and ending resulting from charge diffusion. We can parametrize this behavior by using a smooth step constant with time constant τ_s :

$$f(t) = A \frac{1}{1 + e^{-\frac{t-t_0}{\tau_s}}} e^{-\frac{t-t_0}{\tau_d}} \quad (3)$$

with the step factor, decay factor and their product (i.e., pulse function $f(t)$) indicated in Fig. 3 by the dotted red line, dashed red line and thick black line, respectively.

D. Pulse Function Characteristics

We compare the characteristics of the typical pulse function $f^*(t)$ and the modified pulse function $f(t)$, relating their characteristics to the detected signal. Eq. 2 and 3 are translation invariant; in this subsection we conveniently choose a time origin $t_0 = 0$ to simplify the analysis of the pulse function.

1) *Pulse Height*: We can obtain the relation between pulse height $\max f(t)$ and signal amplitude A by finding t_1 where the first derivative of the pulse function $f(t)$ is zero:

$$\begin{aligned} f^{*'}(t) = 0 &\Rightarrow t_1^* = \tau_s \log \frac{\tau_d + \tau_p}{\tau_p} \\ f'(t) = 0 &\Rightarrow t_1 = \tau_s \log \frac{\tau_d - \tau_s}{\tau_s} \end{aligned} \quad (4)$$

and substituting Eq. 4 into Eq. 2, 3:

$$\begin{aligned} \max f^*(t) &= A \frac{\tau_d}{\tau_d + \tau_p} \left(\frac{\tau_d}{\tau_p} - 1 \right)^{-\frac{\tau_p}{\tau_d}} \\ \max f(t) &= A \frac{\tau_d - \tau_s}{\tau_d} \left(\frac{\tau_d}{\tau_s} - 1 \right)^{-\frac{\tau_s}{\tau_d}} \end{aligned} \quad (5)$$

2) *Pulse Area*: The pulse area can be calculated:

$$\begin{aligned} \int_{-\infty}^{\infty} f^*(t) dt &= A \frac{\tau_d^2}{\tau_d + \tau_p} \\ \int_{-\infty}^{\infty} f(t) dt &= A \pi \tau_s \csc \left(\frac{\pi \tau_s}{\tau_d} \right) \text{ when } \tau_s < \tau_d \end{aligned} \quad (6)$$

where \csc is the cosecant function.

3) *Discussion*: In subsection III-B we show that the step time τ_s changes with location (central or peripheral), thus changing the ratios between fitting parameter A , pulse height, and pulse area. However, using function $f(t)$ for pulse processing allows recovering the position, time and pulse pile-up for each event, without pulse shaping.

For $\{\tau_s, \tau_p\} \ll \tau_d$, the equations above are simplified to:

$$\begin{aligned} \max f(t) &= \max f^*(t) = A \\ \int_{-\infty}^{\infty} f(t) dt &= \int_{-\infty}^{\infty} f^*(t) dt = A \tau_d \end{aligned} \quad (7)$$

E. Two Pulse Pile-up Decomposition

In this experiment we use a single channel SDD, which provides a single waveform for each event. Due to the two apertures and differences in drift time between the central and peripheral areas, the waveforms contain two partially overlapping pulses with amplitudes proportional to the energy of photons detected through each aperture.

To account for the nonzero baseline, clipping of larger signals ($V > 0.3$ V), and the superposition of two pulses with two different amplitudes and arrival times, we extend Eq. 3 to:

$$y(t) = \min \left(y_0 + \frac{A^c \cdot e^{-\frac{t-t_0^c}{\tau_d}}}{1 + e^{-\frac{t-t_0^c}{\tau_s^c}}} + \frac{A^p \cdot e^{-\frac{t-t_0^p}{\tau_d}}}{1 + e^{-\frac{t-t_0^p}{\tau_s^p}}}, y_{max} \right), \quad (8)$$

where the c and p superscripts denote parameters specific for the central and the peripheral aperture, respectively.

Each individual waveform was then fitted (least squares) with the function in Eq. 8, where the signals induced by photons entering through the central and peripheral apertures have amplitudes A^c and A^p , arrival times t_0^c and t_0^p , with 'decay' and 'step' times denoted by τ_d , τ_s^c and τ_s^p , offset y_0 and maximum (clipping) digitized voltages y_{max} . Peak amplitudes for either aperture are collected in histograms.

Fig. 4 shows an example of waveform (red dots) and corresponding least squares fit (black line), with 3 photons entering through the central aperture and 1 photon entering through the peripheral aperture. x

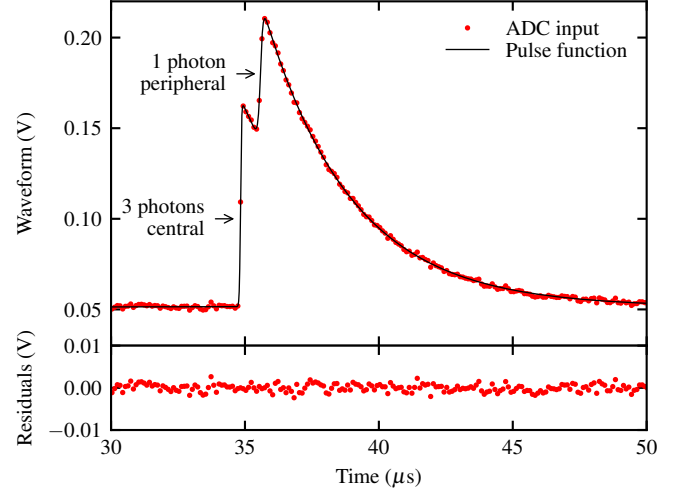


Fig. 4. For each event (i.e., FEL pulse and trigger), fitting (least squares, Eq. 1) central and peripheral aperture traces with their respective amplitudes (A^c and A^p), timing (t_0^c and t_0^p) information, despite pile-up or occasional clipping. This particular trace shows an example with 3 photons entering through the central aperture and 1 photon through the peripheral aperture.

F. Photon Pile-up Statistics at Constant Beam Intensity

For a single line i with average detection rate λ_i , the probability of a pile-up event with j photons in one acquisition is given by the Poisson distribution:

$$P_i^j = P(\lambda_i, j) = \frac{\lambda_i^j e^{-\lambda_i}}{j!} \quad (9)$$

where j is an exponent (unlike elsewhere in this paper, where superscript j is typically an index).

1) *Peak area and detection rate*: The relationship between 1 photon peak area (i.e., detection probability P_i^0) and detection rate λ_i for 1 photon peaks is:

$$P_i^1 = \lambda_i e^{-\lambda_i} \quad (10)$$

For low rates, $\lim_{\lambda_i \rightarrow 0} \lambda_i e^{-\lambda_i} = \lambda_i$, resulting in the usual approximation:

$$\lambda_i \approx P_i^1 \text{ for } \lambda_i \rightarrow 0 \quad (11)$$

However, for relatively high rates in the presence of pile-up, the full form must be used. Solving for λ_i we obtain two solutions:

$$\lambda_i = \begin{cases} -W_0(-P_i^1), & \lambda_i \leq 1 \\ -W_{-1}(-P_i^1), & \lambda_i > 1 \end{cases} \quad (12)$$

where $W_0(x)$ and $W_{-1}(x)$ are the principal and -1 solutions provided by the Lambert-W functions.

Eq. 12 reflects the fact that a 1-photon peak area corresponds to two different rates λ_i on either side of $\lambda_i = 1$ photon/event, thus it is a degenerate measure of photon rate. For low rates ($\lambda_i < 1$ photon/event), the 1 photon peak area can be used; however, for high rates, the pile-up peaks must be considered.

G. Photon Pile-up Statistics with FEL Beams

The self-amplified spontaneous emission process at FELs results in significant pulse-to-pulse intensity variation, often described by a gamma probability distribution function [22]:

$$\Gamma_{PDF}(\alpha, \beta_\Gamma, x) = \frac{\beta_\Gamma^\alpha}{\Gamma(\alpha)} x^{\alpha-1} e^{-\beta_\Gamma x} \quad (13)$$

where Γ is the gamma function, with average rate $\lambda = \alpha\beta_\Gamma$ and shape parameter α . For simplicity we replace β_Γ with λ/α .

The gamma distribution of FEL pulse intensities results in a “stretching” of the Poisson distribution corresponding to the FEL average intensity. The stretching effect resulting from the variability of the FEL beam intensity can be calculated as a weighted average of the Poisson distributions corresponding to different FEL pulse intensities, weighted by their probability:

$$\begin{aligned} \Gamma P_i^j &= \int_0^\infty P(x, j) \Gamma_{PDF}(\alpha, \lambda_i/\alpha, x) dx \\ &= \frac{\lambda_i^j \alpha^\alpha}{(\lambda_i + \alpha)^{\alpha+j}} \frac{\Gamma(\alpha + j)}{j! \Gamma(\alpha)} \end{aligned} \quad (14)$$

(Integrated with [23]). Note that Eq. 14 is a generalized form of the Poisson distribution in Eq. 9, which can be recovered in the limit $\lim_{\alpha \rightarrow \infty} \Gamma P_i^j = P_i^j$. In this paper we used Eq. 14 where applicable; Eq. 9 is provided for reference and should be used for data measured with sources of constant intensity.

1) *Peak area and detection rate*: The relationship between 1 photon peak area (i.e., detection probability P_i^0) and detection rate λ_i for 1 photon peaks results by setting $j = 1$ in Eq. 14:

$$\Gamma P_i^1 = \lambda_i \left(\frac{\alpha}{\lambda_i + \alpha} \right)^{\alpha+1} \quad (15)$$

which can be solved numerically for λ_i . As in Eq. 12, Eq. 15 yields two solutions on either side of $\lambda_i = 1$ photon/event thus the photon pile-up peaks must be considered.

H. Peak Shape

1) *Peak width dependency on energy*: At energy E , the noise r.m.s. is given by the electronic noise σ_0 and an energy dependent noise component (including, i.e., Fano noise) $\sqrt{\sigma_1 E}$, added quadratically:

$$\sigma(E) = \sqrt{\sigma_0^2 + \sigma_1 E} \quad (16)$$

Using this simplified form allows fitting with only two global fitting parameters, σ_0 and σ_1 , resulting in increased fitting stability.

2) *Normal distribution*: We used a normal distribution function for modeling peak shapes of single peaks i (corresponding to the monochromatic lines at energies E_i):

$$\mathcal{N}(E, E_i) = \frac{e^{-\frac{(E-E_i)^2}{2\sigma(E_i)^2}}}{\sqrt{2\pi}\sigma(E_i)} \quad (17)$$

3) *Version 1 generalized normal distribution*: In practice we observe that the peaks display “heavy tails”; we expect this to be specific to this experiment, see subsection IV-B2 for details. To model heavy tails, we use a version 1 generalized normal distribution:

$$\mathcal{N}_1(E, E_i, \beta) = \frac{\beta e^{-\left(\frac{|E-E_i|}{\sqrt{2}\sigma(E_i)}\right)^\beta}}{2\sqrt{2}\sigma(E_i)\Gamma(\frac{1}{\beta})} \quad (18)$$

where β is the shape parameter (e.g., a parameter $\beta = 2$ reverts this function to the normal distribution).

4) *General peak shape*: Combining the two distributions above we obtain the peak function:

$$\mathcal{N}^*(E, E_i) = (1 - \eta)\mathcal{N}(E, E_i) + \eta\mathcal{N}_1(E, E_i, \beta) \quad (19)$$

where η is the fraction of photons in heavy tails.

I. Photon Pile-up Spectra

In this subsection we deduce increasingly complex pile-up spectra: (1) one photon peak spectrum, (2) pile-up of monochromatic line, (3) pile-up of two lines (useful in, e.g., pump-probe experiments), to (4) pile-up of multiple lines.

Note that for all calculated spectra we use probability density functions (PDFs). To obtain histograms from PDFs we multiply the PDF value at each histogram bin position with the number of events N and the histogram bin size.

1) *One photon spectrum (i.e., no pile-up)*: The 1 photon fitting function is the sum of the peaks of L discrete lines and zero peak ($E_0 = 0$):

$$S^1(E) = \sum_{i=0}^L \mathcal{N}(E, E_i) P_i^1 \quad (20)$$

which is subsequently used to fit (least squares) the areas A_i of the N peaks and the background b_j .

2) *Pile-up of a single line (i.e., monochromatic beam)*: The general form for peaks corresponding to j photons from line i is:

$$E_i^j = j E_i \quad (21)$$

The total number of photons detected from line i can be obtained by summation over Eq. 17 with a resulting spectrum:

$$S_i(E) = N \sum_{j=0}^{\infty} \mathcal{N}(E, E_i^j) P_i^j \quad (22)$$

where N is the number of pulses.

3) *Pile-up of two lines*: The photon pile-up of two lines $\{i_1, i_2\}$ can be obtained similarly:

$$E_{i_1 i_2}^{j_1 j_2} = j_1 E_{i_1} + j_2 E_{i_2} \quad (23)$$

The resulting 0 to M photon spectrum is:

$$S_{i_1 i_2}^{0..M} = N \sum_{j_1=0}^M \sum_{j_2=0}^{M-j_1} \mathcal{N}(E, E_{i_1 i_2}^{j_1 j_2}) P_{i_1}^{j_1} P_{i_2}^{j_2} \quad (24)$$

Eq. 24 contains $\binom{M+2}{2}$ terms, resulting from the binomial expansion coefficient:

$$\binom{M+2}{2} = \frac{(M+2)!}{M!2!} \quad (25)$$

4) *Pile-up of multiple lines*: The photon pile-up of L lines $\{i_1, i_2, \dots, i_L\}$ is:

$$E_{i_1 i_2 \dots i_L}^{j_1 j_2 \dots j_L} = \sum_{k=1}^L j_k E_{i_k} \quad (26)$$

The resulting 0 to M photon spectrum is:

$$S_{i_1 i_2 \dots i_L}^{0 \dots M} = N \sum_{j_1=0}^M \sum_{j_2=0}^{M-j_1} \dots \sum_{j_L=0}^{M-\sum_{k=1}^{L-1} j_k} \mathcal{N}(E, E_{i_1 i_2 \dots i_L}^{j_1 j_2 \dots j_L}) \prod_{k=1}^L P_{i_k}^{j_k} \quad (27)$$

Eq. 27 contains $\binom{L+M}{L}$ terms; the algorithm complexity is $O(n!)$, increasing rapidly for large numbers of lines L and photons M .

J. Pile-up Spectrum Fitting and Decomposition

Eq. 27 accurately describes the photon pile-up from multiple lines and could be used for χ^2 fitting of entire spectra. In spectrum fitting we added a third degree polynomial background to the theoretical spectrum:

$$I_{bg}(E) = b_0 + b_1 E + b_2 E^2 + b_3 E^3 \quad (28)$$

The number of counts per histogram bin has a Poisson distribution with an expected error r.m.s. of \sqrt{y} ; we add 1 to account for bins with zero counts, obtaining for each histogram bin an expected error $y_{err} \approx 1 + \sqrt{y}$ (adimensional). This error estimate is used in spectrum fitting.

The variance of the resulting fitting parameters is the principal diagonal of the covariance matrix [24]; its square root yields the fitting parameter r.m.s. error.

Eq. 27 allows obtaining the photon rates λ_i directly, eliminating the need for pile-up deconvolution; the number of photons from each line i is $N\lambda_i$, where N is the number of events observed.

K. Bayesian Decomposition of Single Event Photon Pile-up

The probability that a particular energy E belongs to each of the $\binom{L+M}{L}$ pile-up peaks corresponding to the combinations of M photons and L lines can be calculated from the individual terms of Eq. 27. For example, in the case of $L = 6$, $M = 6$, there are 924 pile-up peaks.

1) *Maximum likelihood estimation of photon pile-up decomposition*: For each detected energy E , we construct a 924 element column vector $\mathbf{P}(E)$, with each of the 924 rows containing the probability that energy E belongs to the 924 corresponding pile-up peaks, calculated from individual terms in Eq. 27.

The $\mathbf{P}(E)$ row with the maximum value indicates the most likely pile-up peak (i.e., maximum likelihood estimator for the pile-up peak).

2) *Error in estimating pile-up peaks*: The estimated error of peak assignment is

$$Err(E) = 1 - \frac{\max \mathbf{P}(E)}{\sum_k \mathbf{P}_k(E)} \quad (29)$$

and the total error is the weighted average of the energy dependent $Err(E)$ with the probability density function of the energy $S(E)$:

$$Err = \int S(E) Err(E) dE \quad (30)$$

This yields the error rate of peak identification.

3) *Error in estimating number of photons*: For estimating the error rate of photon identification, we simulate 10^6 events, with numbers of photons sampled randomly from their respective distributions. For each simulated event we simulate an energy response by sampling one value from the corresponding distribution Eq. 17, and then reconstructed as above. We generate a 6×6 confusion matrix \mathbf{C} , with rows representing simulated photons and columns representing assigned photons after single event pile-up reconstruction.

The error rate of single event Bayesian decomposition of photon pile-up can be calculated from the ratio between the sum of the diagonal and the sum of all cells in confusion matrix \mathbf{C} :

$$Err = 1 - \frac{\sum_i \mathbf{C}_{i,i}}{\sum_{i_r} \sum_{i_c} \mathbf{C}_{i_r, i_c}} \quad (31)$$

4) *Discussion*: Note that the Bayesian maximum likelihood and corresponding error estimates depend strongly on the spectrum characteristics; the methods presented here can be applied to any other pile-up spectrum.

III. PULSE PROCESSING RESULTS

Time results from fitting Eq. 8 are summarized in Fig. 5 with (a) histograms of arrival times (central and peripheral), (b) decay characteristic time (common) and (c) step characteristic times (central and peripheral).

A. Pulse Arrival Times and Interaction Radii

Arrival time results are shown in Fig. 5 (a); the pulse arrival times for the central aperture (black line, $t_0 = 34.842 \pm 0.012 \mu\text{s}$) and peripheral (red line, $t_p = 35.574 \pm 0.037 \mu\text{s}$) are clearly separated.

The difference of 732 ns in pulse arrival times is due to the charge drift time between the SDD periphery and center [25]. The arrival time jitter (12 ns r.m.s. in the center and 37 ns r.m.s. in the periphery) is significantly lower than the difference of arrival times, allowing precise pulse by pulse measurement of arrival times (and corresponding interaction radii), effectively turning the SDD into a position sensitive detector with tens of independent position channels and increasing resolution towards the center.

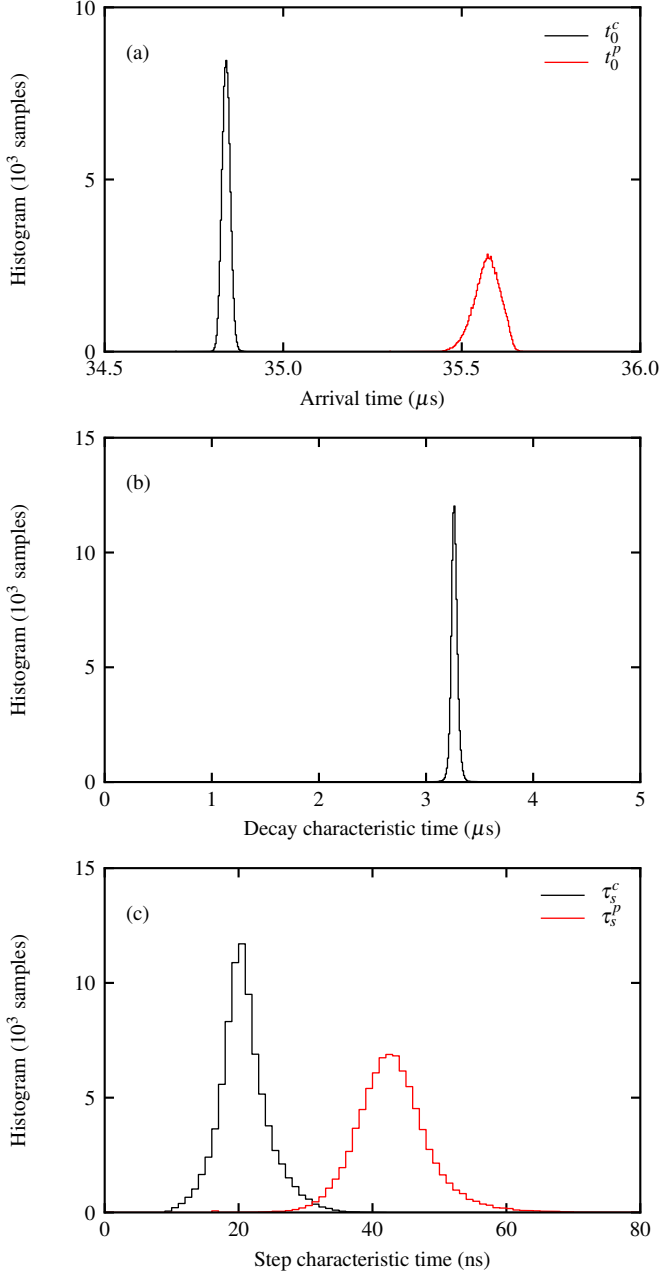


Fig. 5. Distribution of fitting results: (a) shows a histogram of pulse arrival times $t_0^c = 34.842 \pm 0.012 \mu\text{s}$ (black line, central aperture) and $t_0^p = 35.574 \pm 0.037 \mu\text{s}$ (red line, peripheral aperture). The difference of 732 ns is due to the difference of charge drift times and effectively turns the SDD into a position sensitive detector with tens of independent channels and increasing resolution towards the SDD center; (b) shows the histogram of the decay characteristic time $\tau_d = 3.269 \pm 0.035 \mu\text{s}$, corresponding to the nominal 3.2 μs time constant of the high-pass filter of the analog prefilter, and (c) shows the histogram of step characteristic times $\tau_s^c = 21.0 \pm 3.8 \text{ ns}$ (black line, central aperture) and $\tau_s^p = 43.3 \pm 5.9 \text{ ns}$ (red line, peripheral aperture).

B. Decay and Step Characteristic Times

The decay time shown in Fig. 5 (b), $\tau_d = 3.269 \pm 0.035 \mu\text{s}$, corresponds to the nominal 3.2 μs time constant of the high-pass filter of the analog prefilter [21], and has a relatively small variation ($\sigma/\text{mean} \approx 1.1 \%$).

The step characteristic times depicted in Fig. 5 (c) are

clearly different, with a faster step transition in the central compared to the peripheral area; as both signals are processed identically, the difference is due to the supplementary charge diffusion between the periphery and center.

Fitting individual pulses with $f(t)$ (Eq. 8) and analyzing the results shows unambiguously that the photon energy is proportional to the fitting parameter A , while using the pulse height or pulse area results in significantly increased noise. In typical pulse processing, the dependence on peaking time is mitigated by increasing peaking time τ_p through peak shaping, reducing the effect of variations in τ_s . However, using function $f(t)$ for pulse processing allows recovering (without pulse shaping) the time-of-arrival and pulse pile-up for each event.

C. Virtual Multichannel Spectra from Single SDD

Signal amplitudes A^c , A^p resulting from fitting measurements with Eq. 8 are shown in Fig. 6 with a bi-dimensional histogram of the two amplitudes (A^p along the x axis, A^c along the y axis, logarithmic z axis). Multiple clusters of different combinations of energies can be observed.

Fig. 6 inset shows the area corresponding to 1 photon entering through each of the two apertures (in total, 2 photons). Three lines can be identified along each axis, with energies Fe K α (6.40 keV), Fe K β (7.06 keV), and the nominal (9 keV) FEL line. Pile-up of 2 photons sampled from 3 lines each yields $3^2 = 9$ ellipsoids.

The pattern corresponding to Fig. 6 inset repeats, with increasing complexity and (for this photon rate) decreasing intensity, for higher numbers of photons along each of the axes in Fig. 6. However, the pile-up results in clearly separable ellipsoids from each combination of (1) number of photons of each individual energy entering through (2) each of the 2 apertures.

The ellipsoids are more elongated along an axis at $3\pi/4$ (rotated counterclockwise from the x axis), meaning that the sum of the two amplitudes is typically more accurate than the individual amplitudes or their difference. This is to be expected, as the sum of the amplitudes for signals entering through both apertures can be evaluated using many more samples compared to the difference of the amplitudes (limited to the relatively small set of samples between t_0^c and t_0^p , see for example Fig. 4).

D. Response Linearity

To calibrate the gain and offset of the SDD, we selected ellipsoids representing energies resulting only from pile-up of known energies (i.e., Fe K α and Fe K β) and containing at least 100 photons each. This resulted in selecting ellipsoids with up to 3 photons through the central aperture and up to 4 photons through the peripheral aperture.

Fig. 7 shows the centroids of the selected ellipsoids from Fig. 6 (y axis) versus their calculated energy (x axis). Both central and peripheral are stacked on the same plot and are indicated by the large black and small red circles, respectively.

Lines represent corresponding linear fits, with the resulting gains and offsets summarized in Table I. Both fits show good

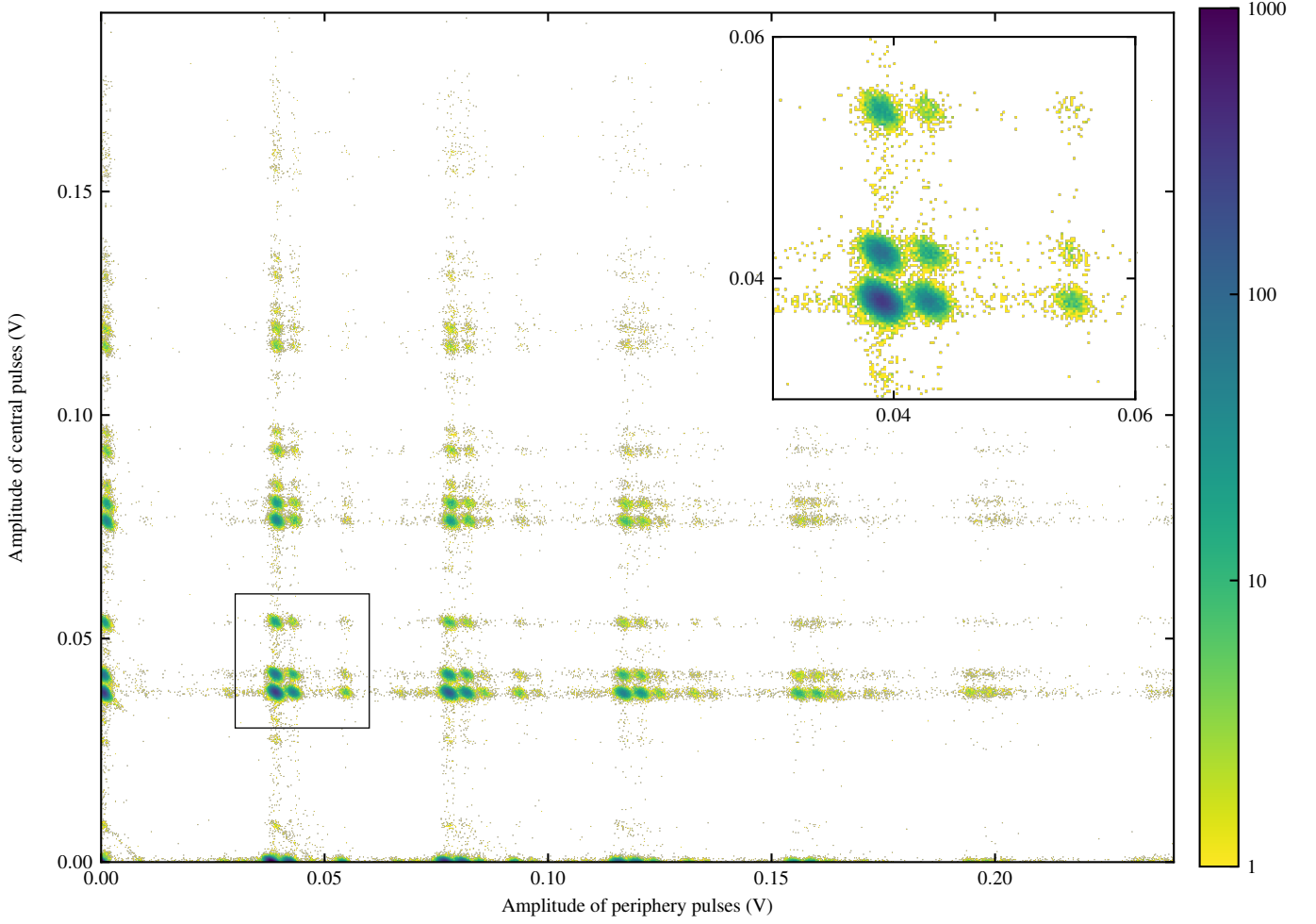


Fig. 6. Each waveform fit yields two amplitudes, A^c and A^p , corresponding to photons entering the SDD through the central and peripheral apertures. Here we show an image (on logarithmic scale) of the bidimensional histogram of these values, A^c along y axis, A^p along x axis); different numbers of photons (0 to 5 photons along x, 0 to 3 photons along y) with different energies (sampled from Fe $K\alpha$ at 6.40 keV, Fe $K\beta$ at 7.06 keV, and FEL beam at ≈ 9 keV) enter through the two apertures yielding a complex histogram; however, the pile-up results in clearly separable ellipsoids from which the number of photons of each individual energy entering through each of the two apertures can be unambiguously reconstructed; the ellipsoids are elongated along an axis at $3\pi/4$, meaning that the sum of the two amplitudes is typically more accurate than the individual amplitudes or their difference; the inset shows a close-up of the area corresponding to one photon entering through each of the two apertures at the 3 different energies (yielding 9 ellipsoids).

TABLE I
GAIN AND OFFSET CALIBRATION

Aperture	Gain (10^{-3} V keV $^{-1}$)	Offset (10^{-4} V)
Central	6.013 ± 0.005	4.838 ± 0.462
Peripheral	6.042 ± 0.006	5.469 ± 0.930

response linearity. The central gain and peripheral gain are similar, with a ratio of 0.995 ± 0.0013 .

IV. PHOTON PILE-UP AND DECOMPOSITION

The amplitudes A^c , A^p resulting from fitting with Eq. 8 were histogrammed to calculate the corresponding spectra.

A. Single Photon Spectrum

In Fig. 8 we show a spectrum of (mostly) single photons (up to 10 keV) entering through either aperture (red dots). The plot

is shown on a square root scale to facilitate the simultaneous visualisation of both intense and weak lines. Along the 3 expected lines, there are a few other lines present.

We fitted this spectrum with a simple model of 7 independent Gaussian peaks (6 fundamental lines plus 1 zero peak) and a third degree polynomial background. This allows us to measure the positions of the peaks, their widths and their areas. Table II lists the fitting parameters and their errors.

Using the peak positions, we identified the six fundamental lines as: Al $K\alpha$, Ti $K\alpha$, Cr $K\alpha$, Fe $K\alpha$, Fe $K\beta$, and the nominal 9 keV line from the FEL beam, and labeled the peaks accordingly. We also determined the beam energy (9.06 keV).

The small peak at ≈ 8 keV does not represent a new fundamental line; it is the pile-up of the Al $K\alpha$ and Fe $K\alpha$ 1 photon peaks. While also $K\beta$ peaks of Al, Ti and Cr must be present, their yield is much lower than the corresponding $K\alpha$ yield; multiplied with their low $K\alpha$ intensity, their contribution

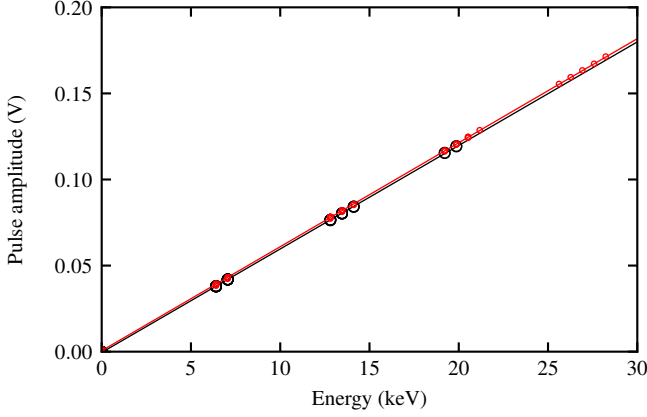


Fig. 7. Circles correspond to the centroids of selected ellipsoids in Fig. 5 (selected for precisely known energies as combinations of Fe $K\alpha$ and Fe $K\beta$ and containing at least 100 photons each); the colors, black and red, represent the central and peripheral apertures, respectively; lines represent corresponding linear fits, with the resulting relationships between energy and pulse amplitudes in Table I; both fits show good response linearity.

TABLE II
FITTING PARAMETERS FOR 1 PHOTON SPECTRUM

Peak	Energy (keV)	Peak area (counts)	Error (counts)	σ (eV)	σ_{error} (eV)
0	0.00	62 469	498	79.01	0.48
Al $K\alpha$	1.49	232	42	91.34	16.23
Ti $K\alpha$	4.63	246	47	104.23	20.59
Cr $K\alpha$	5.31	235	55	200.00	55.05
Fe $K\alpha$	6.40	79 667	564	113.33	0.64
Fe $K\beta$	7.06	16 716	267	127.86	1.77
9 keV	9.06	2932	120	131.88	4.86
χ^2_ν	68.7	reduced chi squared			

can be neglected.

The peak areas in Table II provide a first indication of the intensities of the different peaks; however, using the peak areas as a proxy for the detection rate yields and accurate rate estimation only when each of the λ_i rates is much smaller than 1 photon/event (subsection II-F) and ignoring the FEL distribution of beam intensities (subsection II-G). The peak width estimates have large estimated errors in the peaks with low statistics, and the reduced chi-squared statistic is relatively large ($\chi^2_\nu = 68.7$), due to the “heavy tails”.

This simple, typical analysis illustrates the limitations of using only 1 photon peaks. In next subsection (IV-B) we will address all limitations with an appropriate pile-up fitting model.

B. Photon Pile-up Spectrum and Decomposition

Fig. 9 depicts the entire spectrum of photons entering through either aperture (red dots), up to 37 keV; to facilitate inspection of both intense and weak lines, the plot uses a square root y axis. The 6 fundamental lines (single photons) are clearly visible. Pile-up of multiple photons (up to 5 shown) results in increasing complexity of the detected spectrum and decreasing histogram height (in this particular case).

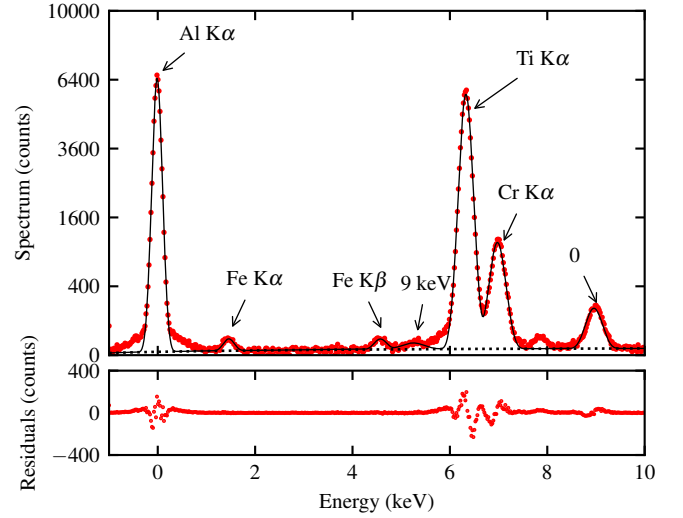


Fig. 8. Red dots show, on a square root y scale, the spectrum of the photons entering through both apertures up to 10 keV; this plot reveals three more discrete energies (between 0 and Fe $K\alpha$) in addition to the three expected ones; black line depicts the least squares fit using 7 Gaussian peaks and a second degree polynomial background (dotted line); this allows us to identify the three small peaks (as Al $K\alpha$, Ti $K\alpha$, and Cr $K\alpha$), and determine the beam energy (9.06 keV); the small peak at ≈ 8 keV is not a new peak, but the convolution of the Al $K\alpha$ and Fe $K\alpha$ peaks; while also $K\beta$ peaks of Al, Ti and Cr must be present, their contribution can be neglected.

TABLE III
FIT PARAMETERS FOR PHOTON PILE-UP SPECTRUM

Parameter	Value	Error	Unit	Details
σ_0	77.9305	0.3984	eV	electronic noise
σ_1	0.7251	0.0079	eV	energy dependent noise
α	16.9168	1.0779		Γ_{PDF} shape
β	0.7742	0.0174		G^* heavy tail shape
η	0.0883	0.0045		G^* heavy tail fraction
$\lambda_{AlK\alpha}$	0.0036	0.0003	photons/event	detection rate
$\lambda_{TiK\alpha}$	0.0049	0.0003	photons/event	detection rate
$\lambda_{CrK\alpha}$	0.0018	0.0003	photons/event	detection rate
$\lambda_{FeK\alpha}$	1.4357	0.0038	photons/event	detection rate
$\lambda_{FeK\beta}$	0.2885	0.0016	photons/event	detection rate
λ_{9keV}	0.0487	0.0007	photons/event	detection rate
χ^2_ν	3.020	reduced chi squared		

The black line depicts the least squares fit using a fitting model with theoretical peak positions of the 7 fundamental lines (zero peak, Al $K\alpha$, Ti $K\alpha$, Cr $K\alpha$, Fe $K\alpha$, Fe $K\beta$, and 9.06 keV), using Eq. 27 with the appropriate changes (substituting Eq. 15 and 19 for Eq. 9 and 17, respectively, to account for the distribution of the FEL beam intensity and the observed “heavy tails” of peaks).

The fit accurately reproduces most features in the data set, resulting in a small reduced chi-squared statistic $\chi^2_\nu = 3.02$ and reproducing all characteristics of the plethora of peaks. Fitting parameters and their errors are detailed in Table III. For the 3 most intense lines (Fe $K\alpha$, Fe $K\beta$, and 9.06 keV) we indexed the peaks with corresponding 3 digit labels. These peaks dominate the higher energy pile-up and can still be clearly separated.

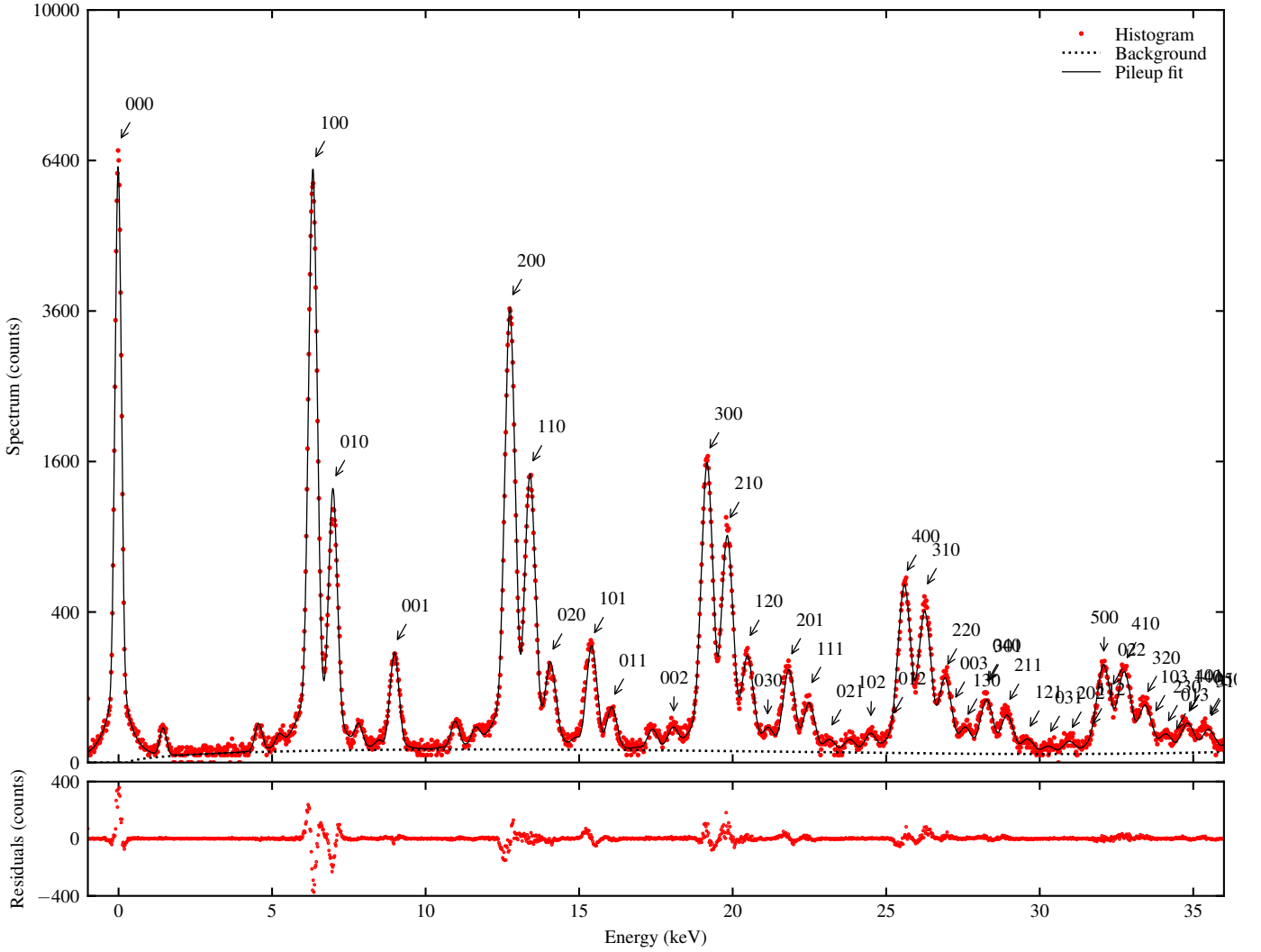


Fig. 9. Red dots show (on a square root y scale) the spectrum of photons entering through both apertures. Black line depicts the least squares fit using the photon pile-up model (Eq. 27 including Eq. 14, 19, 28) with the theoretical peak positions of the 7 fundamental lines (Al K α , Ti K α , Cr K α , Fe K α , Fe K β , and 9.06 keV); fitting yields their individual photon rates λ_i (effectively decomposing the photon pile-up), noise parameters σ_0 and σ_1 (Eq. 16), shape parameter α of the gamma distribution of FEL pulse intensities, “heavy tail” parameters β and η , and a third degree polynomial background (indicated by the dotted black line); the photon pile-up model is remarkably successful in fitting the plethora of peaks, using only the position of fundamental peaks and mathematical modeling. The FEL beam does not have a constant intensity, resulting in a stretching of the Poisson distribution of number of counts (parametrized by Eq. 14). For the 3 most intense lines (Fe K α , Fe K β , and 9.06 keV) we indexed the peaks with corresponding 3 digit labels (representing the number of photons from each of the 3 lines), showing that the photon pile-up model (subsection II-I) accurately describes the measured spectrum ($\chi^2_\nu = 3.020$); overlapping labels indicate overlapping peaks.

1) *Photon rate:* Fitting the pile-up spectrum with the pile-up model yields estimates of photon rates in individual lines (Table III). For peaks with good statistics, the relative error is small (0.27 % for Fe K α and 0.56 % for Fe K β), increasing to 17 % for the peak with lowest statistics, Cr K α .

For the entire spectrum, the most likely photon pile-up decomposition results in a number of photons from each line i of $N\lambda_i$, where N is the number of events. The average total rate $\lambda = \sum \lambda_i = 1.7832 \pm 0.0042$ photons/event, with a majority of Fe K α photons (1.4357 ± 0.0038 photons/event).

2) *Noise:* For Mn K α monochromatic radiation (i.e., 5.89 keV), we obtain a line width of $2.355\sqrt{\sigma_0^2 + \sigma_1 \cdot 5.89 \text{ keV}} = 240 \text{ eV}$ FWHM. The Amptek SDD and PX5 digital pulse processor can yield an energy resolution of $\approx 128 \text{ eV}$ at Mn K α with a peaking time

of 16 μs and acquisition rate of 80 MHz, however, the energy resolution decreases rapidly at shorter peaking times (increasing hyperbolically [10] to 225 eV at $\tau_p = 600 \text{ ns}$ [26]).

The step times we observed in the absence of pulse shaping were an order of magnitude shorter ($\tau_s^c = 21.0 \text{ ns}$ and $\tau_s^p = 43.3 \text{ ns}$) and the Amptek PX5 pulse processor output only provided undersampled waveforms (10 MHz).

On average, we observe a fraction $\eta = 8.8 \%$ of photons in the “heavy tails”, with a distribution shape parameter $\beta = 0.774$ (details in subsection II-H).

The “heavy tails” and a significant fraction of noise are most likely a consequence of undersampling the analog prefilter output (sampling period of 100 ns and characteristic step times of approximately 20 ns to 45 ns), causing noisy estimates of

the strongly correlated τ_s and A (subsection II-D). We expect that a high frequency (e.g., ≥ 100 MHz), direct sampling of the analog prefilter signal will significantly reduce the noise.

3) *FEL statistics*: Using the appropriate model (Eq. 14) which takes into account the gamma distribution of FEL pulses (subsection II-G), we obtain an intensity distribution parameter $\alpha = 16.9$. Note that this parameter is specific to the current experiment and depends on beam characteristics, optics, etc. For reference, a constant intensity beam has a shape $\alpha \rightarrow \infty$.

C. Single Event Bayesian Decomposition of Photon Pile-up

The maximum likelihood decomposition and error estimates depend strongly on the detected spectrum; in this subsection we use the spectrum characteristics obtained in previous subsection (IV-B) and detailed in Table III; we ignored in these estimates the “heavy tails” to estimate error rates that are representative for most SDD setups (including the “heavy tails” increases the error rates by a factor 2.4).

1) *Pile-up peak error*: Fig. 10 shows a single event decomposition approach. Using the method described in subsection II-H, we calculated the probability $S(E)$ of each energy E , depicted in Fig. 10 (a), and with the method described in subsection II-K2 the error probability $Err_{peak}(E)$, shown in Fig. 10 (b). The error rate of peak identification is 1.060 %.

2) *Maximum likelihood decomposition*: For each energy E we estimated the maximum likelihood decomposition in numbers of photons from each line, described in subsection II-K1 and indicated in Fig. 10 (c). Note that both the maximum likelihood decomposition and error estimate depend strongly on the spectrum characteristics (summarized in Table III).

3) *Photon error*: To estimate the error rate in decomposition of photon pile-up, we simulated 10^6 events with characteristics described by Table III, using the method described in subsection II-K3, generating numbers of photons, calculating their pile-up, adding the appropriate noise and then using the maximum likelihood decomposition in subsection II-K1.

We collected the results, for each event, in a confusion matrix, shown in Table IV; rows correspond to simulated photons, while columns correspond to the maximum likelihood decomposition. Cell (i, j) represents how many photons from line i were allocated to line j . Successfully decomposed photons are added to the diagonal. The error rate of photon allocation is 1.019 %. Assuming the same spectrum and a detector operating at the Fano limit, we obtain an error rate of photon allocation of 0.657 %.

4) *Using apertures*: Splitting the pile-up signal in two independent signals using the apertures reduces the photon error rate by avoiding pile-up of large numbers of photons, where the density of pile-up peaks becomes higher. Using two apertures we obtained a reduction in error rate of photon allocation to 0.546 % (and 0.316 % with a detector at the Fano limit).

Splitting the pile-up signal in two also reduces the number of pile-up peaks to consider, increasing computation speed; e.g., for the spectrum discussed here, using $M = 6$ photons guarantees that less than 10^{-4} of the events have more than M counts in one line. Splitting the pile-up signal in two results

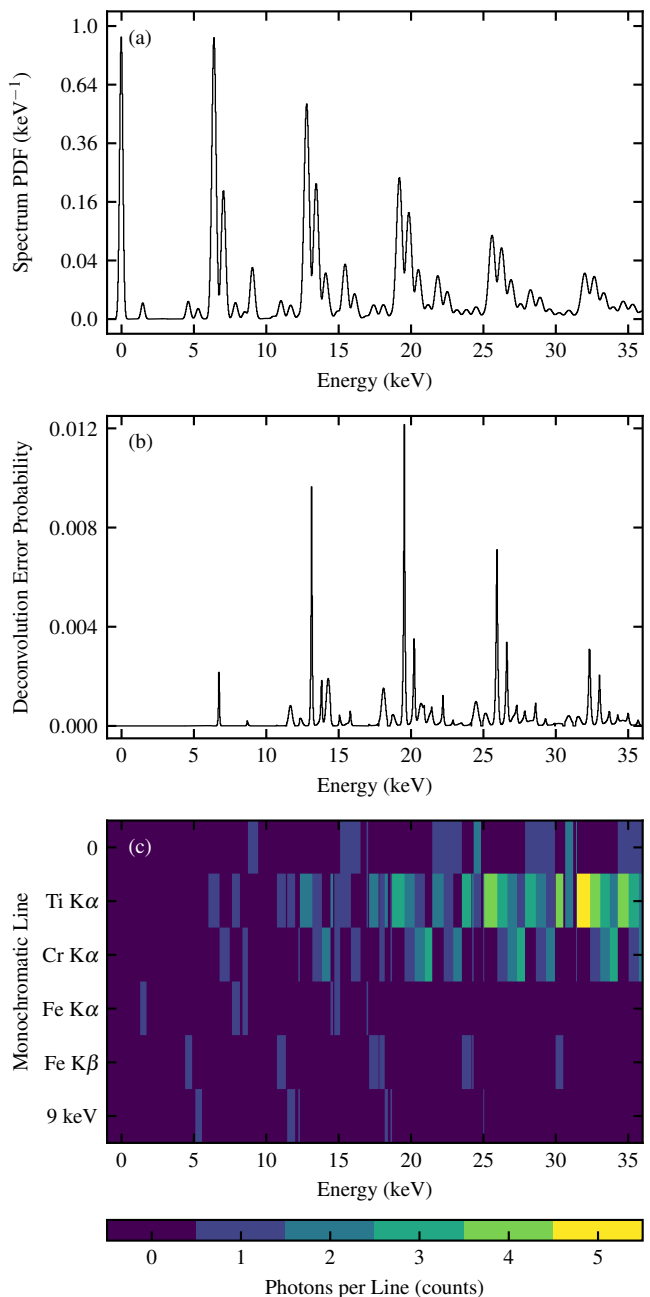


Fig. 10. Pile-up deconvolution of single events: (a) probability density function (PDF) of the incoming spectrum, shown on a square root scale; (b) probability of error in choosing the most likely pile-up peak for each event energy; its integral represents the total error rate, which for this spectrum is 1.072 %; (c) map showing the most likely combinations of numbers of photons in each line for each detected energy.

in a maximum number of photons of $M = 4$. With $L = 6$ lines, this is a reduction from 924 to 210 pile-up peaks while doubling the number of calculations, thus speeding up fitting by a factor 2.2.

V. ePIXS PIXEL DETECTORS: SDD SUCCESSORS

ePixS [27], [28] is a 2D hybrid pixel detector with an array of 10×10 $500 \mu\text{m} \times 500 \mu\text{m}$ pixels, where each pixel has a spectroscopic performance (noise σ of $8 e^-$ or ≈ 30 eV, and measured line width of ≈ 215 eV FWHM at Mn Kα)

TABLE IV
CONFUSION MATRIX OF SINGLE EVENT DECOMPOSITION USING 10^6
SIMULATED EVENTS

	Al K α	Ti K α	Cr K α	Fe K α	Fe K β	9 keV
Al K α	2007	19	1	111	1213	186
Ti K α	1	3642	172	367	141	345
Cr K α	1	97	953	341	171	193
Fe K α	1	95	26	1 375 187	5894	713
Fe K β	39	35	171	5084	273 068	772
9 keV	23	150	62	642	442	45 316
Sum	2073	4037	1384	1 381 731	280 928	47 525

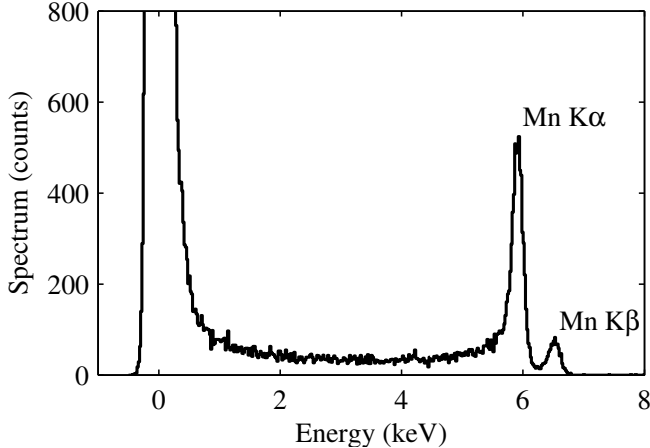


Fig. 11. The ePixS spectroscopic, hybrid pixel detector (reproduced with permission from [30]): ePixS spectrum obtained over all pixels using an ^{55}Fe source, generating characteristic Mn K α (5.9 keV) and Mn K β (6.5 keV) photons, showing the low noise operation with a resulting line width of 225 eV at Mn K α .

approaching that of SDDs. The ePixS camera is built on the ePix platform [29], providing a large number of spectroscopic imaging pixels in a compact, robust and affordable camera package [30].

Fig. 11 shows an ^{55}Fe source spectrum measured with an ePixS detector, yielding Mn fluorescence: Mn K α at 5.90 keV and Mn K β at 6.49 keV (reproduced with permission from [30]). The spectrum is collected in all pixels individually and shown in a single plot here. The ePixS energy resolution is very similar to that in subsection IV-B.

ePixS is a charge integrating pixel detector, providing only the total signal collected by each pixel in each FEL pulse. As a direct result, the pulse processing described in subsections II-C to II-E is not applicable to ePixS. However, the photon pile-up fitting and decomposition are applicable, yielding similar results to those presented here for SDDs.

Pixel detectors are position sensitive (by definition). With 100 pixels, ePixS effectively splits the incoming signal into 100 independent channels, increasing the benefits explained in subsection IV-C4 for two channels. It allows measuring high detector count rates with limited photon pile-up in each pixel.

A single pixel performs similarly with an SDD; 100 pixels allow acquisitions of global rates of $\lambda = 178$ photons/pulse while allowing decomposition into single photons with $\approx 99\%$ accuracy (error rate of 1.019%) and yielding their position.

VI. CONCLUSION

In standard spectroscopy applications there is often a complex spectrum with a multitude of peaks which must be resolved and matched to specific elements.

In contrast, at an x-ray FEL there are often only a few photon energies involved in an experiment, with significant photon pile-up. The discrete spectrum significantly reduces the complexity of pile-up decomposition. SDDs can bring significant contributions at FELs in (1) photon counting, (2) spectrum measurements, and (3) background measurements and set-up optimization.

We present a pulse processing method based on fitting individual, overlapping pulses with pulse functions (a combination of gradual step function and exponential decay) which allows extracting (in the time domain) precise amplitude and timing information in the presence of pulse pile-up and clipping.

We demonstrate that, for individual pulses, the pulse amplitude is not an optimal estimator for signal amplitude (due to variation in peaking times); instead, the pulse amplitude and peaking time are obtained for each pulse by fitting. This removes the need for pulse shaping and takes into account pulse pile-up.

Avoiding pulse shaping reduces peaking times to tens of nanoseconds, resulting in reduced pulse pile-up and allowing decomposition of remaining pulse pile-up at photon separation times down to 100 ns while yielding time-of-arrival information with precision of 10 ns and allows measurements of higher photon rates, compared to typical pulse shaping approaches.

While we demonstrate the usage of this pulse processing method with an SDD and pulsed FEL source, it can be extended to any detector with rapid response (e.g., SDD, transition edge sensors) and x-ray source (e.g., FEL, synchrotron, x-ray tube). In SDDs at pulsed sources, the timing can be used to recover the interaction radii.

At pulsed sources, or at short time intervals between two photons, photon pile-up occurs and the photon rates are not accurately described by the standard proxy, i.e., area of one photon peaks.

Instead, the photon pile-up of a discrete detected spectrum can be accurately described and fitted with the photon pile-up model presented here, yielding precise estimates of the photon rates in individual lines and effectively decomposing the spectrum. We also extended the model to include the stretching of the Poissonian statistics of pile-up introduced by sources with variable intensity (e.g., FELs).

We present a Bayesian decomposition approach which allows accurate decomposition of individual photon energies in single pile-up events, and estimating its error rate in the order of 1% (99% accuracy) for the spectrum discussed in this paper (average rate $\lambda = 1.78$ photons/event, with pile-up of up to 6 photons from 6 monochromatic lines).

The photon pile-up and Bayesian decomposition presented here are useful not only for SDDs but for any applications of pile-up decomposition (e.g., spectroscopy with transition edge sensors [31], low-noise spectroscopic imaging with integrating pixel detectors [32]), or even usual pulse processing with pile-up rejection (two photons with small differences in time-

of-arrival will not be distinguished by the pile-up rejection, resulting in pile-up).

The usefulness of silicon drift detectors will continue into the x-ray FEL era of science. Their successors, the ePixS spectroscopic, hybrid pixel detectors already offer hundreds of pixels with similar performance in a compact, robust and affordable package, particularly useful in x-ray FELs [33].

GLOSSARY

ADC:	Analog-to-digital converter
CSPAD:	Cornell-SLAC pixel array detector
CXI:	Coherent X-ray Imaging instrument at LCLS
DAC:	Digital-to-analog converter
ePix:	SLAC hybrid pixel detector platform
ePixS:	Spectroscopic pixel detector in the ePix family
FEL:	Free-electron laser
FWHM:	Full width at half maximum ($\approx 2.355 \sigma$)
LCLS:	Linac Coherent Light Source at SLAC
PDF:	Probability density function
r.m.s.:	Root mean square
SDD:	Silicon drift detector
SLAC:	SLAC National Accelerator Laboratory
XPP:	X-ray Pump-Probe instrument at LCLS

ACKNOWLEDGMENT

Use of the Linac Coherent Light Source (LCLS), SLAC National Accelerator Laboratory, is supported by the U.S. Department of Energy, Office of Science, Office of Basic Energy Sciences under Contract No. DE-AC02-76SF00515.

We applied the SDC approach for the sequence of authors [34]. Statement of authorship: conception, C. J. Kenney and G. Blaj; LCLS beamtime principal investigator, G. Carini; ePixS ASIC design, A. Dragone; design and acquisition of data, all authors; analytical methods, G. Blaj; analysis, G. Blaj; drafting the manuscript, G. Blaj; revising the manuscript: C. J. Kenney.

REFERENCES

- [1] E. Gatti and P. Rehak, "Semiconductor drift chamber — an application of a novel charge transport scheme," *Nuclear Instruments and Methods in Physics Research*, vol. 225, no. 3, pp. 608 – 614, 1984. [Online]. Available: [https://dx.doi.org/10.1016/0167-5087\(84\)90113-3](https://dx.doi.org/10.1016/0167-5087(84)90113-3)
- [2] P. Emma, R. Akre, J. Arthur, R. Bionta, C. Bostedt, J. Bozek, A. Brachmann, P. Bucksbaum, R. Coffee, F.-J. Decker, Y. Ding, D. Dowell, S. Edstrom, A. Fisher, J. Frisch, S. Gilevich, J. Hastings, G. Hays, P. Hering, Z. Huang, R. Iverson, H. Loos, M. Messerschmidt, A. Miahnahri, S. Moeller, H.-D. Nuhn, G. Pile, D. Ratner, J. Rzepiela, D. Schultz, T. Smith, P. Stefan, H. Tompkins, J. Turner, J. Welch, W. White, J. Wu, G. Yocky, and J. Galayda, "First lasing and operation of an ångström-wavelength free-electron laser," *Nature Photonics*, vol. 4, no. 9, pp. 641–647, 2010. [Online]. Available: <https://dx.doi.org/10.1038/nphoton.2010.176>
- [3] H. Graafsma, "Requirements for and development of 2 dimensional x-ray detectors for the European x-ray free electron laser in Hamburg," *Journal of Instrumentation*, vol. 4, no. 12, p. P12011, 2009. [Online]. Available: <https://dx.doi.org/doi:10.1088/1748-0221/4/12/P12011>
- [4] G. Blaj, P. Caragiulo, G. Carini, S. Carron, A. Dragone, D. Freytag, G. Haller, P. A. Hart, R. Herbst, S. Herrmann, J. Hasi, C. J. Kenney, B. Markovic, K. Nishimura, S. Osier, J. Pines, J. Segal, A. Tomada, and M. Weaver, "Detector development for the Linac Coherent Light Source," *Synchrotron Radiation News*, vol. 27, no. 4, pp. 14–19, 2014. [Online]. Available: <https://dx.doi.org/10.1080/08940886.2014.930803>
- [5] G. Blaj, P. Caragiulo, G. Carini, S. Carron, A. Dragone, D. Freytag, G. Haller, P. Hart, J. Hasi, R. Herbst, S. Herrmann, C. J. Kenney, B. Markovic, K. Nishimura, S. Osier, J. Pines, B. Reese, J. Segal, A. Tomada, and M. Weaver, "X-ray detectors at the Linac Coherent Light Source," *Journal of Synchrotron Radiation*, vol. 22, no. 3, pp. 577–583, 2015. [Online]. Available: <https://dx.doi.org/10.1107/S1600577515005317>
- [6] B. Nasri, C. Fiorini, A. Grande, F. Erdinger, P. Fischer, and M. Porro, "A front-end stage with signal compression capability for XFEL detectors," *Journal of Instrumentation*, vol. 10, no. 01, p. C01022, 2015. [Online]. Available: <https://doi.org/10.1088/1748-0221/10/01/C01022>
- [7] G. Blaj, C. J. Kenney, S. Boutet, G. Carini, M. Chollet, G. Dakovski, G. Haller, P. Hart, S. Herrmann, J. Koglin, M. Messerschmidt, S. Nelson, J. Pines, S. Song, J. Thayer, A. Tomada, and G. Williams, "Performance of silicon drift detectors at the LCLS," in *2016 IEEE Nuclear Science Symposium and Medical Imaging Conference (NSS/MIC)*. IEEE, 2016, in press.
- [8] R. Wilson, "V. noise in ionization chamber pulse amplifiers," *The London, Edinburgh, and Dublin Philosophical Magazine and Journal of Science*, vol. 41, no. 312, pp. 66–76, 1950.
- [9] L. Wielopolski and R. P. Gardner, "Prediction of the pulse-height spectral distortion caused by the peak pile-up effect," *Nuclear Instruments and Methods*, vol. 133, no. 2, pp. 303–309, 1976. [Online]. Available: [https://doi.org/10.1016/0029-554X\(76\)90623-6](https://doi.org/10.1016/0029-554X(76)90623-6)
- [10] R. Redus, *Digital Pulse Processors, Theory of Operation*, Amptek Inc, 2009. [Online]. Available: <https://amptek.com/pdf/dpp%5Ftheory.pdf>
- [11] S. Rozen, "Pile up rejection circuits," *Nuclear Instruments and Methods*, vol. 11, pp. 316–320, 1961. [Online]. Available: [https://doi.org/10.1016/0029-554X\(61\)90031-3](https://doi.org/10.1016/0029-554X(61)90031-3)
- [12] R. P. Gardner and L. Wielopolski, "A generalized method for correcting pulse-height spectra for the peak pile-up effect due to double sum pulses: Part I. predicting spectral distortion for arbitrary pulse shapes," *Nuclear Instruments and Methods*, vol. 140, no. 2, pp. 289–296, 1977. [Online]. Available: [https://doi.org/10.1016/0029-554X\(77\)90297-X](https://doi.org/10.1016/0029-554X(77)90297-X)
- [13] L. Wielopolski and R. P. Gardner, "A generalized method for correcting pulse-height spectra for the peak pile-up effect due to double sum pulses: Part II. the inverse calculation for obtaining true from observed spectra," *Nuclear Instruments and Methods*, vol. 140, no. 2, pp. 297–303, 1977. [Online]. Available: [https://doi.org/10.1016/0029-554X\(77\)90298-1](https://doi.org/10.1016/0029-554X(77)90298-1)
- [14] M. Nakhoshtin, Z. Podolyak, P. Regan, and P. Walker, "A digital method for separation and reconstruction of pile-up events in germanium detectors," *Review of Scientific Instruments*, vol. 81, no. 10, p. 103507, 2010. [Online]. Available: <https://doi.org/10.1063/1.3499241>
- [15] W. Guo, R. P. Gardner, and C. W. Mayo, "A study of the real-time deconvolution of digitized waveforms with pulse pile up for digital radiation spectroscopy," *Nuclear Instruments and Methods in Physics Research Section A: Accelerators, Spectrometers, Detectors and Associated Equipment*, vol. 544, no. 3, pp. 668–678, 2005. [Online]. Available: <https://doi.org/10.1016/j.nima.2004.12.036>
- [16] E. Gatti, M. Sampietro, and P. Manfredi, "Optimum filters for detector charge measurements in presence of 1/f noise," *Nuclear Instruments and Methods in Physics Research Section A: Accelerators, Spectrometers, Detectors and Associated Equipment*, vol. 287, no. 3, pp. 513 – 520, 1990. [Online]. Available: [https://dx.doi.org/10.1016/0168-9002\(90\)91571-R](https://dx.doi.org/10.1016/0168-9002(90)91571-R)
- [17] D. A. Van Dyk and H. Kang, "Highly structured models for spectral analysis in high-energy astrophysics," *Statistical Science*, pp. 275–293, 2004. [Online]. Available: <https://doi.org/10.1214/088342304000000314>
- [18] J. E. Davis, "Event pileup in charge-coupled devices," *The Astrophysical Journal*, vol. 562, no. 1, p. 575, 2001. [Online]. Available: <https://doi.org/10.1086/323488>
- [19] M. Chollet, R. Alonso-Mori, M. Cammarata, D. Damiani, J. Defever, J. T. Delor, Y. Feng, J. M. Glowina, J. B. Langton, S. Nelson, K. Ramsey, A. Robert, M. Sikorski, S. Song, D. Stefanescu, V. Srinivasan, D. Zhu, H. T. Lemke, and D. M. Fritz, "The X-ray Pump-Probe instrument at the Linac Coherent Light Source," *Journal of Synchrotron Radiation*, vol. 22, no. 3, pp. 503–507, May 2015. [Online]. Available: <https://doi.org/10.1107/S1600577515005135>
- [20] S. Boutet and G. Williams, "The Coherent X-ray Imaging (CXI) instrument at the Linac Coherent Light Source (LCLS)," *New Journal of Physics*, vol. 12, no. 3, p. 035024, 2010. [Online]. Available: <https://dx.doi.org/10.1088/1367-2630/12/3/035024>
- [21] Amptek Inc., *PX5 User Manual and Operating Instructions*. Bedford, Massachusetts: Amptek Inc., 2016.
- [22] M. Hogan, C. Pellegrini, J. Rosenzweig, S. Anderson, P. Frigola, A. Tremaine, C. Fortgang, D. Nguyen, R. Sheffield, J. Kinross-Wright *et al.*, "Measurements of gain larger than 10^5 at $12 \mu\text{m}$

- in a self-amplified spontaneous-emission free-electron laser,” *Physical Review Letters*, vol. 81, no. 22, p. 4867, 1998. [Online]. Available: <https://doi.org/10.1103/PhysRevLett.81.4867>
- [23] Wolfram Research, “Mathematica,” Champaign, Illinois, 2017, version 11.1.
- [24] P. Richter, “Estimating errors in least-squares fitting,” Telecommunications and Data Acquisition, NASA, Jet Propulsion Laboratory, Tech. Rep. 42-122, 1995. [Online]. Available: https://ipnpr.jpl.nasa.gov/progress_report/42-122/122E.pdf
- [25] J. Segal, J. Plummer, and C. Kenney, “Simulation of charge cloud evolution in silicon drift detectors,” in *Nuclear Science Symposium, 1996. Conference Record., 1996 IEEE*, vol. 1. IEEE, 1996, pp. 558–562. [Online]. Available: <https://doi.org/10.1109/NSSMIC.1996.591061>
- [26] Amptek Inc., “XR-100SDD performance, fig. 7,” 2017. [Online]. Available: <http://amptek.com/products/xr-100sdd-silicon-drift-detector/#7>
- [27] J. Hasi, G. Blaj, P. Caragiulo, A. Dragone, G. Haller, P. Hart, R. Herbst, C. J. Kenney, B. Markovic, K. Nishimura, S. Osier, J. Pines, J. Segal, and A. Tomada, “High channel count x-ray spectroscopy detector for x-ray FELs,” talk presented at the Synchrotron Radiation Instrumentation 2015 Conference, New York, NY, Jun 2015.
- [28] A. Dragone, P. Caragiulo, B. Markovic, G. Blaj, J. Hasi, J. Segal, A. Tomada, K. Nishimura, R. Herbst, P. Hart, S. Osier, J. Pines, C. J. Kenney, and G. Haller, “ePixS: a high channel count x-ray spectroscopy detector for x-ray FELs,” 2015, talk presented at the IEEE Nuclear Science Symposium and Medical Imaging Conference (NSS/MIC), San Diego, CA, Nov 2015.
- [29] A. Dragone, P. Caragiulo, B. Markovic, R. Herbst, K. Nishimura, B. Reese, S. Herrmann, P. A. Hart, G. Blaj, J. Segal, A. Tomada, J. Hasi, G. Carini, C. J. Kenney, and G. Haller, “ePix: a class of front-end ASICs for second generation LCLS integrating hybrid pixel detectors,” in *2013 IEEE Nuclear Science Symposium and Medical Imaging Conference (2013 NSS/MIC)*. IEEE, Oct 2013, pp. 1–5. [Online]. Available: <https://dx.doi.org/10.1109/NSSMIC.2013.6829505>
- [30] K. Nishimura, G. Blaj, P. Caragiulo, G. Carini, A. Dragone, G. Haller, P. Hart, J. Hasi, R. Herbst, S. Herrmann, C. J. Kenney, M. Kwiatkowski, B. Markovic, S. Osier, J. Pines, B. Reese, J. Segal, A. Tomada, and M. Weaver, “Design and performance of the ePix camera system,” *AIP Conference Proceedings*, vol. 1741, no. 1, p. 040047, 2016. [Online]. Available: <https://dx.doi.org/10.1063/1.4952919>
- [31] K. Irwin and G. Hilton, *Transition-Edge Sensors*. Berlin, Heidelberg: Springer, 2005, ch. 3, pp. 63–150. [Online]. Available: <https://dx.doi.org/10.1007/10933596%5F3>
- [32] G. Blaj, P. Caragiulo, A. Dragone, G. Haller, J. Hasi, C. J. Kenney, M. Kwiatkowski, B. Markovic, J. Segal, and A. Tomada, “X-ray imaging with ePix100a, a high-speed, high-resolution, low-noise camera,” *SPIE Proceedings*, vol. 9968, pp. 99 680J–99 680J–10, June 2016. [Online]. Available: <https://dx.doi.org/10.1117/12.2238136>
- [33] G. Blaj, P. Caragiulo, G. Carini, A. Dragone, G. Haller, P. Hart, J. Hasi, R. Herbst, C. J. Kenney, B. Markovic, K. Nishimura, J. Pines, J. Segal, C. Tamma, and A. Tomada, “Future of ePix detectors for high repetition rate FELs,” *AIP Conference Proceedings*, vol. 1741, no. 1, p. 040012, 2016. [Online]. Available: <https://dx.doi.org/10.1063/1.4952884>
- [34] T. Tschardt, M. E. Hochberg, T. A. Rand, V. H. Resh, and J. Krauss, “Author sequence and credit for contributions in multiauthored publications,” *PLoS Biol*, vol. 5, no. 1, p. e18, 2007. [Online]. Available: <https://doi.org/10.1371/journal.pbio.0050018>